C-nanocoated ZnO by TEMPO-oxidized cellulose templating for improved photocatalytic performance

He Xiao, Yiwei Shan, Wenyao Zhang, Liulian Huang, Lihui Chen, Yonghao Ni, Bruno Boury, Hui Wu

1 **C-nanocoated ZnO by TEMPO-oxidized Cellulose Templating for**

2 **Improved Photocatalytic Performance**

3

4 **He Xiao [a], Yiwei Shan [a], Wenyao Zhang [c], Liulian Huang [a], Lihui Chen [a], Yonghao Ni [a,d],**

5 **Bruno Boury [b*], Hui Wu [a*]**

6

7 [a] College of Material Engineering, Fujian Agriculture and Forestry University, Fuzhou, 350108,

8 China

9 [b] Institute Charles Gerhardt UMR CNRS 5253, CMOS team, Université de Montpellier, CC1701,

10 place E. Bataillon, 34095, Montpellier, France

11 [c] Department of Chemical Engineering, University of Waterloo, Waterloo, Ontario N2L3G1,

12 Canada

13 [d] Limerick Pulp and Paper Centre, Department of Chemical Engineering, University of New

14 Brunswick, Fredericton, NBE3B 5A3, Canada

15

16 Corresponding authors: Bruno Boury (bruno.boury@univ-montp2.fr), Hui Wu

17 (wuhuifafu@163.com)

18

19 **Abstract**

20 Ultrafine C-doped ZnO/carbon nanocomposites with different photocatalytic activities

21 have been prepared using TEMPO-oxidized cellulose as a template but also as the

22 source of carbon. The result is an enhancement of the photocatalytic activity ascribed

23   to different phenomena: a high mesoporosity beneficial to mass transport, a thin

24   carbon layer onto ZnO increasing the charge transfer and hydrophobicity of ZnO, a

25   narrowing of ZnO band gap and an increase of the zinc (V_{Zn}) and oxygen (V_o)

26   vacancies effectively suppressing of the charge recombination. These are evidenced

27   by photocatalytic test of photodegradation of methyl orange (MO) achieved to assess

28   and compared the different photocatalysts. The highest rate constant value of

29   photodegradation of MO is 0.0254 min^{-1}, three times higher than that of ZnO prepared

30   without templates (0.0087 min^{-1}). The present results introduce a new vision of the

31   use of template with multiple roles in the preparation of inorganic materials and

32   specially photocatalysts.

33

34   **Keywords:** ZnO; Cellulose; Photocatalyst; Template; Carbon coating.

35

36   **Introduction**

37   Heterogeneous photocatalysis is one of the most promising processes for

38   pollution control as well as production of chemicals and fuels(Dong et al., 2015; Lee,

39   Lai, Ngai & Juan, 2016; Qu & Duan, 2013; Zhou, Yu & Jaroniec, 2014). Apart from

40   TiO$_2$ and few others, ZnO is one of the most popular and promising semiconductors

41   with high photocatalytic potential. It is now well documented that large exciton

42   binding energy (60 meV), low price and low toxicity are advantages of ZnO, while

43   major limitations are a wide band gap (3.37 eV), a high recombination rate of

44   photoinduced electron–hole pairs and a photocorrosion with formation of zinc

2

45   hydroxide(Spathis, 1995). Among the different strategies reported to overcome these

46   drawbacks, achieving nanosizing of ZnO particles is the simplest way to increase the

47   proportion of active sites of the photocatalyst by increasing the specific surface area.

48   This nanosizing also hampers the electron-hole recombination by shortening the

49   diffusion path up to the surface of the photogenerated state. Other strategies to

50   improve the photocatalytic activity, such as nanosizing of ZnO particles can be

51   associated with the presence of metal, metal oxide or sulfide particles(Vaiano,

52   Matarangolo, Murcia, Rojas, Navio & Hidalgo, 2018). Besides, combining this

53   nanosizing with an assembly of carbon (C) to obtain a ZnO/C nanocomposites is

54   emerging as the most attractive approach(Han, Yang, Weng & Xu, 2014). Carbon

55   presents the desired electrical and photophysical properties acting as a temporary

56   photoelectron reservoir to store and shuttle the photogenerated electrons from the

57   semiconductor(Li & Cao, 2011; Samadi, Shivaee, Zanetti, Pourjavadi & Moshfegh,

58   2012; Yang & Xu, 2013; Zhang, Zhang, Tang & Xu, 2012). Carbon is also envisaged

59   to improve the adsorption capability of the photocatalyst surface while improving its

60   chemical stability as an efficient shield against corrosion.

61   However, these properties can deeply vary depending on the C polymorph, e.g.

62   carbon nanotube, graphite, fullerene, graphene. Secondly, fairly different effects can

63   be expected depending on the proportion and location of carbon, varying from a true

64   doping of the ZnO crystal structure with an effect on the band gap(Yu, Zhang & Peng,

65   2016), or a photosensitization of the ZnO semiconductor(Hewlett & McLachlan,

66   2016), or a hydrophobization of the surface with modification of the adsorption

3

67   capacity(Hong, Lee & Ko, 2011; Yang, Weng & Xu, 2013, 2014).

68   Therefore, the C polymorph and its nanoassembly with ZnO are the keys for

69   photocatalytic activity. Numerous ways to do so already exist, but there is still a need

70   for improvements in terms of performances, sustainability, safety and cost. In this

71   context, biopolymers are increasingly used as template and C-precursors(Boury &

72   Plumejeau, 2015; Foresti, Vazquez & Boury, 2017).   The interest in such biopolymer

73   template ability of relies on their efficiency to bind metal cations and achieve an

74   efficient control over the particle size of ZnO during sol-gel or solvothermal processes.

75   Furthermore, although they are removable by calcination, these biotemplates are

76   easily converted into highly porous C upon pyrolysis. So far, work in this area has

77   targeted either the complete elimination of the template upon calcination, or its

78   complete transformation into carbon upon pyrolysis. As we shall see below, we

79   hereby propose an intermediate situation. Beside water-soluble polysaccharides like

80   starch (Cheng, Ji, Wu & Zhang, 2016; Patrinoiu et al., 2016), alginic acid(Cheng et al.,

81   2018), agarose (Tran, 2016)or cellulose acetate(Olaru, Calin & Olaru, 2014; Ye,

82   Zhang, Liu & Zhou, 2011), the water insoluble cellulose is the cheapest and most

83   available polysaccharide. In addition, it is not strategical for food supply, and useful

84   for the preparation of ZnO(Lefatshe, Muiva & Kebaabetswe, 2017; Liu, Yao, Wang &

85   Ma, 2017; Yuan et al., 2017; Zhao, Zuo, Guo & Pan, 2017) and many other metal

86   oxides(Boury & Plumejeau, 2015; Foresti, Vazquez & Boury, 2017). Due to the high

87   hydroxyl content and the presence of very few carboxylic/ate functions in its fibril

88   surface, cellulose can efficiently coordinate metal cations(O'Connell, Birkinshaw &

4

89   O'Dwyer, 2008; Olivera, Muralidhara, Venkatesh, Guna, Gopalakrishna & Kumar,

90   2016; Wu, Lu, Zhang, Yuan, Xiong & Zhang, 2013; Xiong, Lu, Wang, Zhou & Zhang,

91   2013). Interestingly, increasing such naturally low carboxylic/ate content of natural

92   celluloses is now easily achievable thanks to the development of the regioselective

93   oxidation of the primary alcohol function in C6 position into a carboxylic function

94   using the mixture of the following reagents: NaOCl/NaBr/2,2,6,6-tetramethyl

95   piperidine-1-oxyl known as TEMPO. This chemical modification to increase the

96   carboxylic function of cellulose has recently been reported for example to enhance the

97   mineralization of cellulose with hydroxyapatite for bone tissues engineering

98   (Abouzeid, Khiari, Beneventi & Dufresne, 2018; Safwat et al., 2018). We thought that

99   this could also be an advantage in the case of the mineralization by ZnO and could

100   afford an efficient pathway to better control the nucleation process of ZnO. We have

101   reported the benefit of TEMPO-oxidized cellulose over pristine cellulose(Xiao, Zhang,

102   Wei & Chen, 2018), the improvement in photocatalytic activity was attributed to the

103   higher specific surface area obtained by controlling the growth of ZnO particles. The

104   presence of a very low level of C was also suspected of acting as a doping agent

105   lowering the ZnO band gap. At that point, we thought possible and attractive to

106   modify the preparation of the material in order to achieve a deeply different

107   nanoassembly of ZnO and C, this time targeting a true C coating of the ZnO different

108   from a C-doping. Thanks to the use of ultrasonication during the sol-gel processing of

109   ZnO templated by TEMPO-oxidized cellulose and to a careful control over the

110   temperature during the calcination that preserve a thin layer of C, we are now able to

111 report here the formation of a C-coated ZnO with very high photocatalytic activity.

112 The general strategy of preparation of the samples is summarized in Figure 1, in

113 addition to the complete characterization of materials, we present a comprehensive

114 study of the photocatalytic process of degradation with methyl orange, an

115 identification of the role of the C layer and a comparison with other C-doped ZnO.

116

117 **Materials and methods**

118 *Materials*

119 Zinc nitrate hexahydrate ($Zn(NO_3)_2 \cdot 6H_2O$), urea (CH_4N_2O), sodium hypochlorite

120 (NaClO), sodium bromide (NaBr) and sodium hydroxide (NaOH), hydrochloric acid

121 (HCl) and ethanol (CH_3CH_2OH) were of analytical grade and utilized without

122 purification. The above chemicals were acquired from Shanghai Macklin Biochemical

123 Co.,Ltd. 2,2,6,6-tetramethylpiperidine-1-oxyl (TEMPO) agent (≥98%) and methyl

124 orange (MO) (≥96%) were obtained from Aladdin Industrial Corporation. Bamboo

125 dissolving pulp (α-cellulose ≥94%) was obtained from Fujian Qingshan Paper

126 Industry Co., Ltd and was used without pretreatment before experiment.

127

128 *Preparation of TEMPO-oxidized cellulose (TOC)*

129 The TEMPO-oxidized cellulose was prepared from bamboo pulps according to the

130 previously reported method(Sehaqui, Zhou, Ikkala & Berglund, 2011): Bamboo pulp

131 (2.00 g) was suspended in deionized water (200 mL) at room temperature (25 °C)

132 using mechanical stirring (400 r/min) for 1 h. Then TEMPO agent (0.04 mmol g^{-1} of

133 dried cellulose) and sodium bromide (NaBr, 0.4 mmol g^{-1} of dried cellulose) were

134 successively added into the above suspension. Then, sodium hypochlorite (NaClO, 12

135 mmol g^{-1} of dried cellulose) was added dropwise to the mixture. During the

136 TEMPO-oxidized process, the pH of the mixture was maintained at 10 by adding

137 NaOH (0.1 M) with continuous stirring for 6 h. The obtained suspension was

138 homogenized by sonication（FS-1200N）at 25°C for 5 min with ultrasonic power

139 (1000W), and then centrifuged at 9000 r min^{-1} for 15 min. The solid residue was

140 recovered, and impurities were thoroughly washed through abundant dilute

141 hydrochloric acid (0.1 M) and deionized water repeatedly. The as-prepared sample,

142 labeled as TOC, was stored at 4°C as an aqueous dispersion for further experiments.

143 Non-oxidized cellulose of bamboo dissolving pulp was denoted as NOC. Carboxyl

144 contents in the different cellulose were determined by the electric conductivity

145 titration method(Jiang & Hsieh, 2013).

146

147 *Preparation of TOC-templated ZnO (TOC-ZnO) and template-free ZnO (FT-ZnO) and*

148 *cellulose-templated ZnO (NOC-ZnO)*

149 TEMPO-oxidized cellulose TOC (1.89 g, 11.67 mmol, 1wt % water suspension) was

150 dispersed in 100 mL deionized water for 30 min at room temperature (25°C). After

151 that, Zn(NO$_3$)$_2$.6H$_2$O (2.97 g, 10 mmol) was previously dissolved in 40 mL deionized

152 water, then added into the TOC suspension with continuous stirring (400 r/min) for 1

153 h at 25 °C. Subsequently, urea (0.36 g, 6 mmol, 0.6 mol L^{-1} water solution) was

154 dropwise added into the mixtures with ultrasonic process (FS-1200N, 1000 W, 25°C)

155 for 5 min, then heated in an oil bath at 90°C for 3 h leading to the formation of a white

156 suspension. The latter was then repeatedly washed with 500 mL deionized water five

157 times in a row, centrifuged at 8000 r min^{-1} and vacuum dried at 60 °C for 24 h labeled

158 as TOC-ZnO. For comparison, pure ZnO and ZnO/unmodified cellulose composites

159 were prepared according to the same procedure as described above FT-ZnO and

160 NOC-ZnO, respectively.

161

162 *Preparation of calcined sample TOC-ZnO^x, (x = 300, 400, 500, 600) and TF-ZnO^{400}*

163 *and NOC-ZnO^{400}*

164 TOC-ZnO were calcined at different temperatures (300°C, 400°C, 500°C, 600°C) in

165 muffle furnace in steady conditions without any air stream or addition for 2 h and then

166 cooled down quickly in laboratory atmosphere leading to samples respectively labeled

167 as TOC-ZnO^{300}, TOC-ZnO^{400}, TOC-ZnO^{500} and TOC-ZnO^{600}. TF-ZnO and NOC-ZnO

168 were similarly calcined at 400°C in air atmosphere for 2 h denoted as TF-ZnO^{400} and
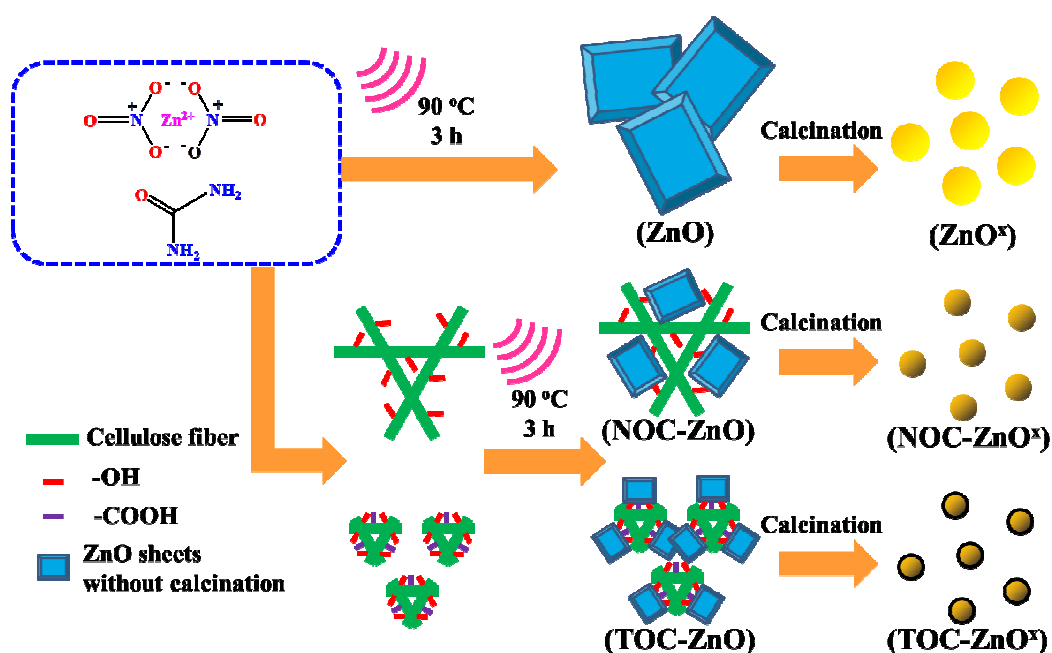
169 NOC-ZnO^{400}, respectively.

170

Fig.1. Schematic illustration of the concept and general procedure for the preparation of

C-covered ZnO nanocrystals templated by TEMPO-oxidized cellulose.

173

Photocatalyst characterization

TEMPO-oxidized cellulose was analyzed by fiber analyzer (Techpap，MorFi

Compact，France) to characterize the length and width. Fourier transform infrared

(FT-IR) spectra were measured by an FT-IR spectrometer equipped with an ATR

accessory (Pekin-Elmer, 1600, USA) ranging the wavelength from 4000 cm^{-1} to 400

cm^{-1}. The zeta potential of 0.1 wt% aqueous bamboo dissolving pulp (NOC) and

TEMPO-oxidized cellulose (TOC) suspensions were recorded with a Zetasizer Nano

ZS90 analyzer (Malvern, Britain). The thermogravimetric analysis (TGA) curves were

performed using STA-449 thermogravimetric analyzer (Netzsch, Germany) with a

temperature range of 25-700ºC at a heating rate of 10 ºC·min^{-1} in air flow (50

mL·min^{-1}). Raman scattering spectra were recorded on Invia Reflex Raman

185 Microscopy (Renishaw, UK) equipped with a 532 nm laser source. X-ray diffraction

186 (XRD) analyses were recorded out by X-ray diffractometer (Rigaku, Ultima Ⅳ, Japan)

187 using Cu Kα radiation, tube voltage 40 kV and tube current 45 mA. Contact angle

188 testing was measured by a dynamic drop tension meter (DSA 30, KRUSS, Germany).

189 ZnO-based photocatalysts were coated and adhered to slide glasses with tapes. Then 5

190 µL of water drop was placed on the surface of the photocatalysts to investigate the

191 contact angle. A field emission scanning electron microscope (Hitachi, SU8010, Japan)

192 was used to observe the morphologies of carbon-doping ZnO samples. The detailed

193 microstructures of ZnO nanocrystals were investigated by using a transmission

194 electron microscopy (JEOL, JEM-2100, Japan) with a field emission gun operating at

195 200 kV. The chemical compositions of ZnO nanocrystals were determined by energy

196 dispersive spectroscopy (HORIBA, XMX 1011, Japan). Total organic carbon content

197 of calcined samples was measured by elemental analyzer (Vario EL cube, Elementar,

198 Germany). X-ray photoelectron spectra (XPS) were measured using an ESCALAB

199 250 instrument (Thermo Scientific, USA) with Al Kα radiation monochromatic source.

200 The valence band (VB) values were detected by XPS scanning from 0~10 eV with

201 0.05 eV recording once. The specific surface area and pore characteristics of ZnO

202 nanocrystals were determined by N_2 adsorption-desorption measurements

203 (Micromeritics, ASAP 2020, USA). Diffuse reflectance UV-Vis (DR UV-Vis) spectra

204 were recorded on Cary 500, Varian Corporation. Electron paramagnetic resonance

205 (EPR) measurements were carried out by an EMXnano spectrometer (Bruker,

206 Germany) operating at 77 K with a frequency of 9.4 GHz. The photoluminescence

207 spectroscopy (PL) spectra of the samples were recorded using LS55

208 spectrophotometer (Perkin-Elmer, USA) with 325 nm excitation wavelength. The

209 electrochemical impedance spectroscopy measurement was performed at VersaSTAT

210 MC electrochemical workstation (Princeton, USA). The measurement was carried out

211 in a three-electrode cell with a glassy (FTO) carbon electrode as the working electrode,

212 Ag/AgCl as the reference electrode and Pt plate as the counter electrode.

213

214 *Evaluation of photocatalytic activity*

215 The ultraviolet light source is a 6 W lamp with the wavelength range of 200-400 nm

216 (Beijing Zhong Jiao Jin Yuan Technology Co., Ltd.). And the distance between the

217 light source and the reaction tube was fixed as 10 cm(Zhao, Zuo, Guo & Pan, 2017).

218 ZnO-based photocatalyst (25 mg, 0.309 mmol) were added into methyl orange

219 solution (5 mg L^{-1}, 100 mL) with continuously stirring (300 r/min) at $25^{o}C$ for 30 min

220 in dark conditions in order to reach the adsorption-desorption equilibrium. Then, light

221 irradiation was turned on and aliquots (4 mL) were withdrawn and filtered through

222 PES membrane (Jin Teng Experimental Equipment Co., Ltd., 13×0.22 μm, 0.22 μm

223 pore size, Tianjin, China) at 15 min, 30 min, 60 min, 90 min and 120 min, respectively.

224 The MO concentration of the filtrate was measured by UV-Vis spectrophotometer

225 (Shimadzu, UVmini-1240, Japan) at 463 nm. To investigate the photocatalytic

226 stability of TOC-ZnO^{400} was used in five consecutive cycles with centrifugal

227 separation (washing by deionized water three times and vacuum drying at $40^{o}C$ for 12

228 hours) after each one. The XRD characterization of the photocatalyst after five cycles

11

229 was also detected by X-ray diffractometer.

230

231 **Results and discussion**

232 *Synthesis and Characteristics of TOC-ZnO, FT-ZnO and NOC-ZnO.* Submicron fibrils

233 of bamboo pulp cellulose were used for controlling morphology, porosity and growth

234 of ZnO nanoparticles. Prior to reaction with zinc nitrate in urea solution, selective

235 oxidation of the primary alcohol in the C6 position was performed with TEMPO in

236 basic medium to increase the carboxylic/ate content(Isogai, Saito & Fukuzumi, 2011;

237 Pierre et al., 2017). Using the electric conductivity titration method, the proportion of

238 this group in TOC was estimated to 1.51 mmol g^{-1}, much higher than the initial

239 proportion of 0.1 mmol g^{-1} for NOC. This significant increase in the number of

240 carboxylate groups is a decisive element allowing a greater control of the intermediate

241 ZnO growth in the form of a nanoparticle more homogeneously distributed along the

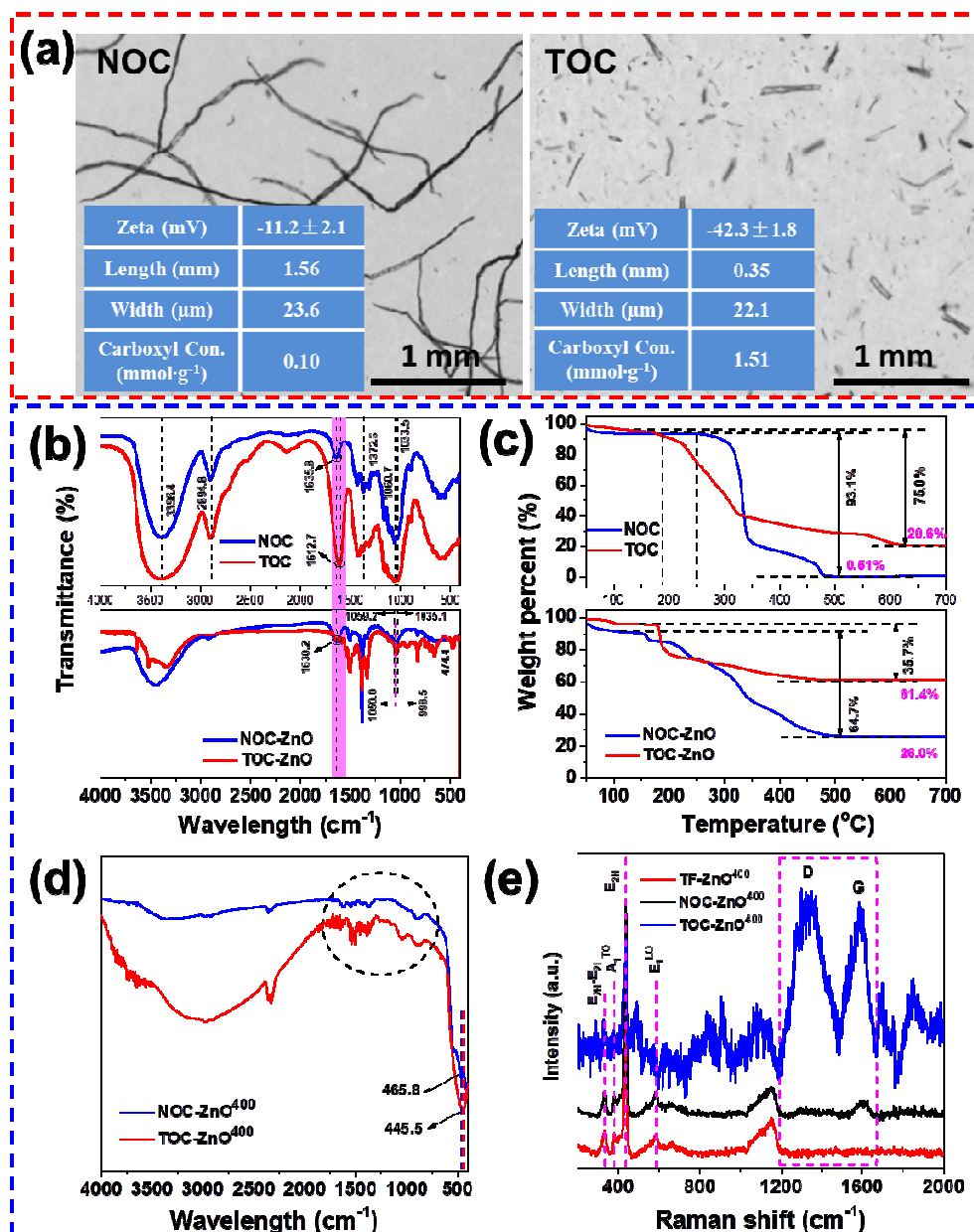242 fibers (see calculation of this distribution in Table S1).

Fig.2 Images and main characteristics of pure cellulosic fibers and TOC (a), FT-IR spectra of cellulosic fibers and ZnO samples (b), Thermograms of cellulosic fibers NOC and TOC and of ZnO samples (c), FT-IR spectra of ZnO[400] samples (d), Raman spectra of three different ZnO[400] samples (e).

The size and morphologies of cellulose fibers before and after TEMPO-oxidized treatment are shown in Figure 2-a,b. As observed by other(Cao, Ding, Yu & Al-Deyab,

251 2012), it is clear that the TEMPO treatment results in a shortening of the length of

252 pristine cellulose (NOC), the latter being frequently ten times longer than the

253 whiskers-like TEMPO-oxidized cellulose (TOC). However, the average width is

254 apparently not modified by the TEMPO treatment. Thus, it indicates that the side

255 reactions of TEMPO oxidation that lead to chain scission occurred mainly in some

256 specific part of the fibers resulting in their scission and subsequent length reduction.

257 The amorphous domains of the cellulose fiber are candidates for this as observed in

258 other chemical treatment of cellulose, e.g. acidic hydrolysis. A consequence of the

259 chemical modification is an important decrease of the Zeta potential from -11.2 mV

260 for NOC to -42.3 mV for TOC resulting from the increase of anionic carboxylate

261 groups on the surface of the TEMPO-oxidized cellulose.

262   The ZnO-containing materials were prepared by solvothermal process in mild

263 condition (3 h, 90°C) either without cellulose, or with cellulose or with

264 TEMPO-oxidized cellulose (Figure 1). The FTIR spectra of NOC and TOC are

265 compared in Figure 2-b. Several characteristic peaks are similar, especially those at

266 3396.4 cm^{-1}, 2894.8 cm^{-1} and 1372.6 cm^{-1} respectively due to O-H and C-H stretching

267 vibrations and C-H asymmetric deformations. Besides, the C-O stretching vibrations

268 are slightly shifted from 1060.7 cm^{-1} for C to 1033.5 cm^{-1} for TOC. However, the

269 major difference between both samples is the position and intensity of the C=O

270 stretching frequency of carboxylate groups of NOC (1635.8 cm^{-1}) and TOC (1612.7

271 cm^{-1}), both phenomena being related to the TEMPO oxidation. For NOC-ZnO the

272 characteristic peak at 1059.2 cm^{-1} and 1035.1 cm^{-1} are respectively assigned to

273   glucose ring skeletal vibration and C-O stretching vibration peak. These bands are

274   shifted for TOC-ZnO respectively to 1049.1 cm^{-1} and 992.3 cm^{-1}, this being ascribable

275   to H-bonding between cellulose and oxo- or hydroxo-Zn species in nanoparticles(Ali

276   et al., 2016). Due to the limit of the spectrometer, the maximum of band absorption

277   for the stretching mode of ZnO at 431 cm^{-1} is not observed.

278   To evaluate the relative proportions of cellulose and ZnO in the TOC composite,

279   thermogravimetry analysis was performed on NOC, TOC, NOC-ZnO and TOC-ZnO,

280   (Figure 2-c). Weight loss starts earlier for TOC (180-190°C) than for NOC (250°C),

281   this results from possible esterification of the abundant carboxylic and hydroxyl

282   groups in TOC compared to NOC. It can also be ascribed to dehydration between

283   residual Zn(OH) functions. For NOC alone, a 99.5% weight loss by 700°C is

284   measured, much higher than the weight loss for TOC, of up to 79.4%. This is ascribed

285   to the presence of sodium carboxylate and its decomposition upon pyrolysis result in

286   sodium oxide. When nano-assembled with ZnO, the situation is very different, and

287   TGA curves reveal that a much higher proportion of ZnO is assembled with TOC

288   (40.8% yield at 700°C for TOC-ZnO) compared with NOC (25.5% yield at 700°C for

289   C-ZnO). Additionally, these analyses indicate that the decomposition of cellulose is

290   almost complete by 500°C. Indeed, after thermal treatment at 400°C, FTIR analysis in

291   figure 2-d shows tiny peaks ranged from 1800 to 1000 cm^{-1} that cannot be attributed

292   to ZnO and are ascribed to carbonaceous residue issued from NOC or TOC. The Zn-O

293   stretching vibration peaks at 465.8 cm^{-1} for NOC-ZnO^{400} and 445.5 cm^{-1} for

294   TOC-ZnO^{400} are blue-shifted compared to the TF-ZnO^{400} (474.4 cm^{-1}), which is

295   ascribable to the smaller crystal size after the template preparation process(Yu, Chen,

296   Wang & Yao, 2015).

297   To further investigate the characteristics of the samples, the Raman spectra of

298   TF-ZnO^{400} (Figure 2-e) show that four main peaks at 331.4 cm^{-1}, 380.8 cm^{-1}, 437.4

299   cm^{-1} and 584.4 cm^{-1} were assigned to E_{2H}-E_{2L}, A_1^{TO}, E_{2H} and E_1^{LO}, respectively. In the

300   spectra of NOC-ZnO^{400} and TOC-ZnO^{400}, the peaks of E_{2H}-E_{2L}, A_1^{TO} and E_1^{LO} are all

301   blue-shifted, respectively 329.5 cm^{-1} and 326.2 cm^{-1} for E_{2H}-E_{2L}, 378.9 cm^{-1} and 374.8

302   cm^{-1} for A_1^{TO} and finally 582.6 cm^{-1} and 574.4 cm^{-1} for E_1^{LO}. A possible explanation is

303   the presence of a doping phenomenon as frequently reported to explain blue shift in

304   metal oxides like ZnO(Beltran, Barrero & Punnoose, 2019). Carbon arising from the

305   residue of cellulose is one candidate as evidenced by EDX analyses given below.

306   Besides, an important feature of the Raman spectrum of TOC-ZnO^{400} is the presence

307   of two dominant peaks at approximately 1340 cm^{-1} and 1590 cm^{-1}, usually attributed

308   to D and G signals of graphitic carbon structure. The broadness and the low intensity

309   of the signals indicate two important points: first the thinness of the carbon domain,

310   and secondly the highly disordered structure of the graphitic carbon. An expected

311   situation if considering the low temperature of calcination. However, this is clearly

312   different from NOC-ZnO^{400} and TF-ZnO^{400} for which no signal in these regions are

313   observed.

314   The EDX analysis confirms the effect of the cellulosic oxidized template on the

315   composition of the material, namely the presence of residual carbon: 1.09% in

316   TOC-ZnO^{400}, 0.47 % in NOC-ZnO^{400} and only 0.23% in TF-ZnO^{400}, given in Fig.S1.

317 In the latter, the total organic carbon from quantitative element analysis gives slightly

318 different values: 0.45% in TOC-ZnO^{400}, higher than 0.14% for NOC-ZnO^{400} and

319 0.05% for TF-ZnO^{400}. Surface contamination by CO_2 and carbonate-related species

320 can explain the higher values obtained by EDX. However, the high C-contents are

321 clearly related to the use and decomposition of cellulosic template, samples were

322 gold-coated for analysis. The presence of such residual carbon is further demonstrated

323 below by the TEM images. This can result from the fact that tiny parts of the

324 cellulosic template are not fully accessible to oxygen and are carbonized but not

325 further oxidized into CO_2 and water. This phenomenon is favored by the relatively

326 low temperature of calcination used here (400°C) and the absence of any air stream in

327 the furnace, however, the reason why the TEMPO-oxidized cellulose leads to higher

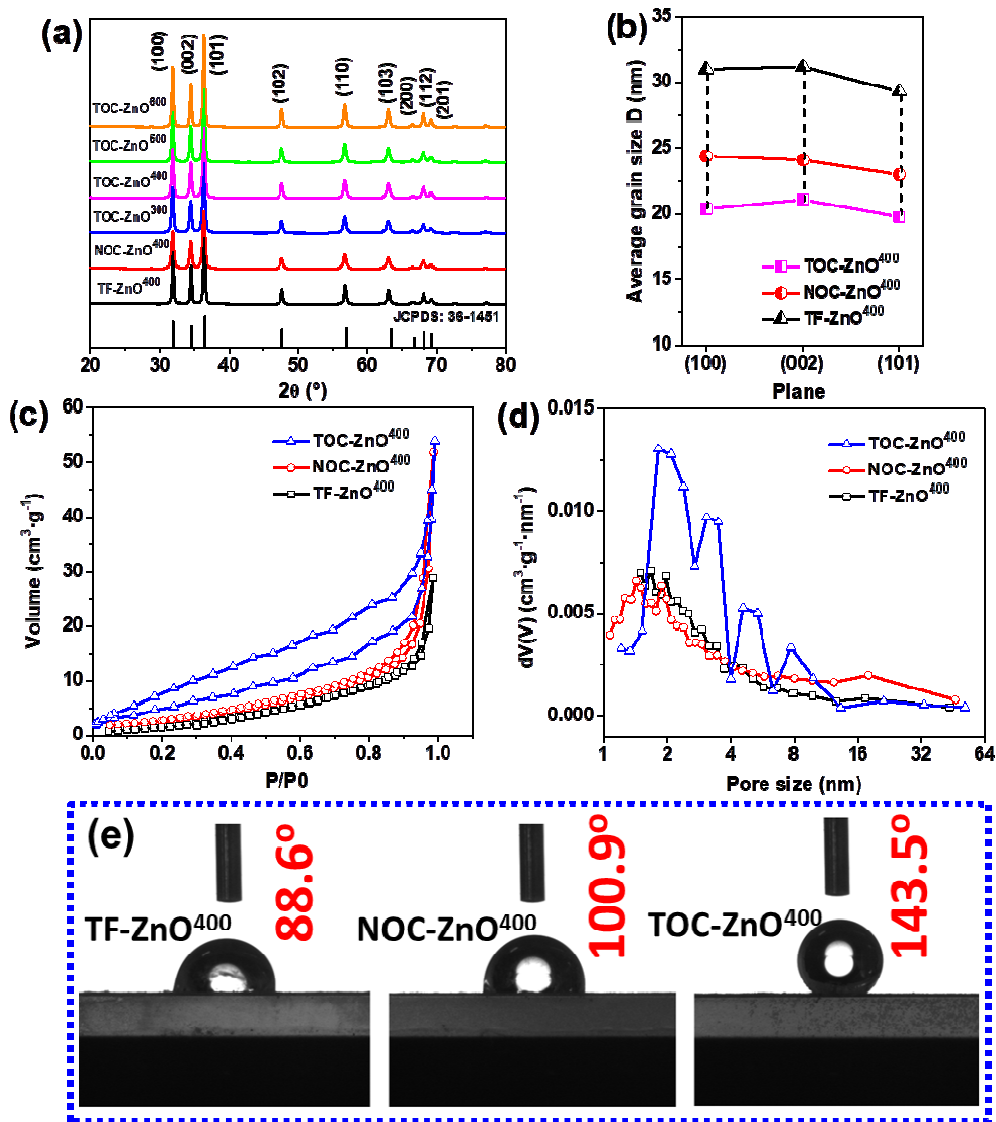328 C-content is not understood at present.

329

Fig.3 Powder XRD patterns of samples after calcination (a) and average grain size (D) of (100),

(002) and (101) for TF-ZnO[400], NOC-ZnO[400] and TOC-ZnO[400] (b), N_2 adsorption-desorption

isotherms (c), pore size distribution derived from desorption isotherm of TF-ZnO[400], NOC-ZnO[400]

and TOC-ZnO[400] (d) and micrographs of contact angles measurements of TF-ZnO[400],

NOC-ZnO[400] and TOC-ZnO[400] (e).

335

For all the samples, the X-ray diffraction pattern is in good accordance with the

characteristic of the hexagonal wurtzite structure ZnO (JCPDS 36-1451) with

338 characteristic peaks at 31.90º, 34.56º, 36.40º, 47.68º, 56.74º, 63.00º, 66.50º,68.08º,

339 69.22º indexed to (100), (002), (101), (102), (110), (103), (200), (112), (201) planes

340 respectively (Figure 3a, Table S2). However, the TOC-ZnO without calcination

341 contained ZnO with lower crystallinity as evidenced in Fig.S2. Moreover, other

342 signals of the patterns could be attributed to zinc(II) hydroxocarbonate $[Zn_4(OH)_6CO_3]$

343 (PDF: 19-1458). The presence of the latter is important for further understanding of

344 the evolution, characteristics and performances of the material after calcination.

345   The effect of cellulose template on the properties of ZnO is also revealed by the

346 values of specific surface area, pore volume and pores distribution obtained from

347 nitrogen porosimetry measurements and shown in Figure 3c, d and Table S3. The

348 adsorption-desorption isotherms of TF-ZnO^{400}, NOC-ZnO^{400} and specially

349 TOC-ZnO^{400} corresponded to the type IV curve with a H3 hysteresis loop, which

350 confirms the mesoporous nature of all the samples probably arising from intergranular

351 voids. From Figure 3d, as supported by the broad hysteresis loop, TOC-ZnO^{400} is

352 clearly less microporous than TF-ZnO^{400} and NOC-ZnO^{400} showing an important

353 proportion of pore with $\varnothing$<2 nm, and a higher proportion of mesopores 2 <$\varnothing$<≈20 nm.

354 From Table S3, the specific surface area and pore volume of as-prepared ZnO samples

355 was as follows: TF-ZnO^{400}<NOC-ZnO^{400}< TOC-ZnO^{400}. There are four possible

356 driving forces for the formation of mesopores. Part of it can initially originate from

357 inter-particles voids left between the vicinal nanoparticles attached to cellulose, this

358 can be seen as an effect of the cellulose hard templating. Secondly, during the

359 calcination, these nanoparticles are prevented from collapse and sintering by the

360 presence of the carbon residues and layer (Fig.S1) that also can result in mesoporosity.

361 Thirdly, either during the hydrothermal process, or during the calcination if some urea

362 residues are included in the pre-calcined ZnO nanoparticles, their decomposition

363 generates CO_2 can also result in pore formation. This can also occur during the

364 thermal decomposition of the Zinc(II) hydroxocarbonate (identified in X-ray

365 diffraction pattern, Fig. S2) that is evidenced before calcination, and which

366 decomposition can occur by multistep mechanisms (see in Fig.S3). Another effect of

367 the use of TOC instead of NOC is a deep change of the hydrophobic/hydrophilic

368 balance of the material surface. As shown in Figure 3e, the contact angles of

369 TOC-ZnO^{400} (143.5º) were far larger than TF-ZnO^{400} (88.6º) and NOC-ZnO^{400}

370 (100.9º) demonstrating the higher hydrophobicity of the surface of TOC-ZnO^{400} and

371 an additional evidence of its specificity. However, the powder formed stable mixture

372 in solution of the photocatalytic test as the result of the stirring and possibly of a light

373 photocatalytic oxidation of the C-layer taking place during the beginning of the test

374 and leading to a reduced hydrophobicity.

375 As a primary conclusion on the synthesis of the photocatalyst, it is possible to

376 underline the major effect and advantages of TOC as template in the synthesis of ZnO.

377 First, TOC combined with ultrasonic activation severely limits the growth of ZnO

378 nanocrystals. The abundant carboxyl/ate groups of the TOC probably act as efficient

379 Zn(II) binding sites that increase the number of seeding sites and decrease the ZnO

380 particles size and their aggregation. The massive elimination of TOC upon calcination

381 leads to higher specific surface area and porous volume, both beneficial to drive high

382   mass transfer during the photocatalytic process. However, the low temperature of

383   calcination (400°C) allows preserving a thin carbon layer coating the ZnO

384   nanocrystals.

385   The average grain size determined using typical crystal planes (100), (002) and

386   (101) for TF-ZnO[400] are found to be similar ≈30 nm (Figure 3b). The average grain

387   size of the characteristic planes of NOC-ZnO[400] and TOC-ZnO[400] is lower by 22%

388   and 33% respectively. This indicates that a cellulose template is very effective in

389   reducing crystal growth and agglomeration of primary grains, especially if

390   carboxylate groups have been increased like in TOC as expected; the peak positions

391   of (100), (002) and (101) have negatively shifted with the increase of the temperature

392   of calcination but the average grain size increase by 10-50% in Table S2. Such 2θ

393   shift is attributed at present to the presence of carbon, either as a C-layer or a

394   C-doping, that can generate strain upon calcination. It has been reported that for a

395   nanocrystalline material subjected to a strain, diffraction peaks can be either

396   broadened (due to nonuniform strain, "strain broadening") and/or shift toward high-2θ

397   value (for uniform compressive strain) or low-2θ value (for uniform tensile
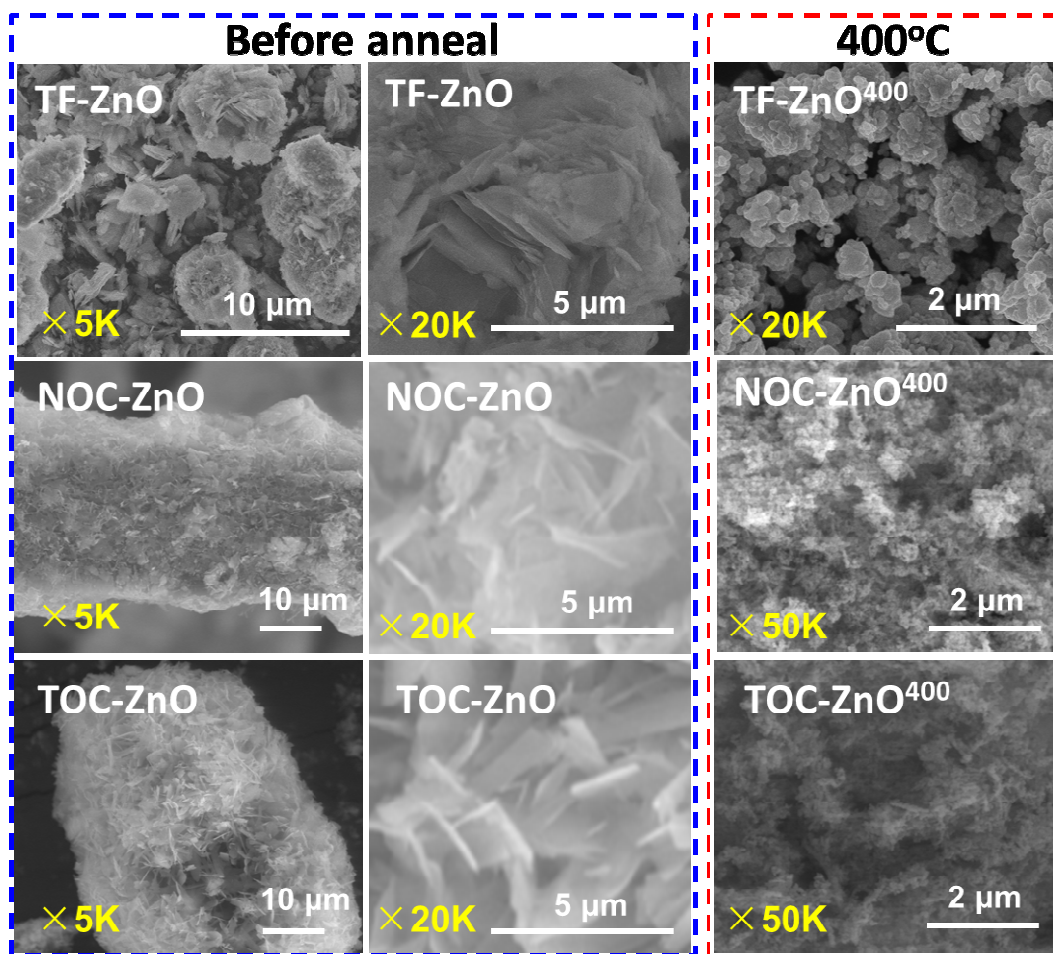
398   strain)(Cullity, 1978).

Fig.4 SEM images of TF-ZnO, NOC-ZnO and TOC-ZnO before and after thermal treatment at 400ºC.

The effect of the cellulose on the morphology of ZnO is evidenced by SEM analysis of samples before calcination (Figure 4) and has consequences on the sample afterward. As shown in Figure 4, large and disordered flake-like aggregates (2~4 µm) of ZnO are obtained in the absence of any template. The presence of NOC or TOC results in a uniform deposit of smaller flakes on the surface of the cellulose template; interestingly they are smaller when using TOC (~1 µm) rather than NOC (1~2 µm). After calcination and removal of the cellulosic template, the original aggregates are

410 transformed. The calcination introduces major modifications with the increase of the

411 temperature (300~600ºC) as shown in Fig.S4; especially, the ZnO morphologies

412 change from flakes to nanorods and to coarse rounded nano- and macro-particles,

413 their size gradually increasing with temperature.(Li, Lan, JianPing, XiaoSong, HaiYan

414 & JinYan; Zhao, Zuo, Guo & Pan, 2017). This modification of morphology

415 corresponds, at least partially, with the thermal decomposition of loose flake-like

416 basic zinc carbonate [$Zn_4(OH)_6CO_3$] resulting in ultrafine ZnO with classical nanorod

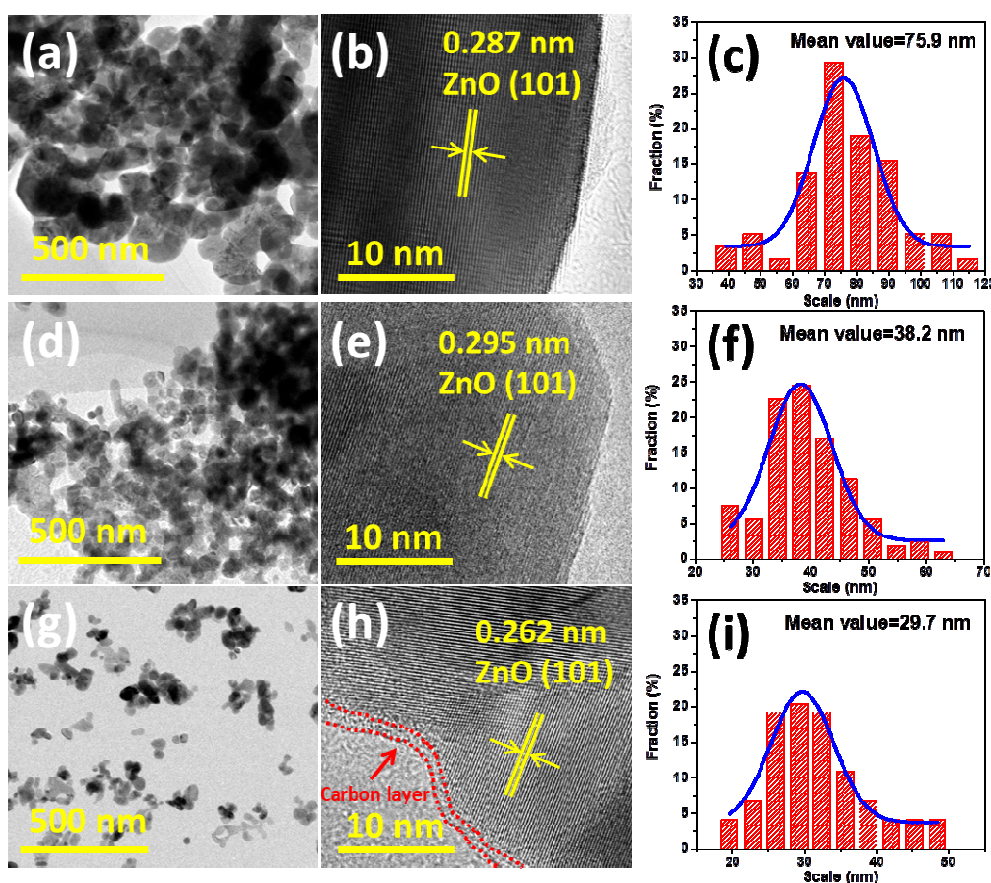417 morphology.

418

419 **Fig.5** TEM images and particle size distribution of TF-ZnO[400] (a, b and c), NOC-ZnO[400] (d, e and

420 f), and TOC-ZnO[400] (g, h and i).

421

23

422   At lower scale, TEM images (Figure 5) further demonstrate the effect of the

423   cellulosic template. When absent, the corresponding sample FT-ZnO[400] presents ZnO

424   nanoparticles size ≈40-200 nm (average size=75.9 nm), much larger than the

425   nanoparticle size of NOC-ZnO[400] and TOC-ZnO[400] ≈20-100 nm. Both values are

426   higher than the crystallite size determined by X-ray analysis suggesting that the

427   particles may not be completely crystallized or made of several crystallites. Beside the

428   size decreasing with the effect of cellulose template, lattices fringes have also

429   narrowed. In Figure 5-b and 5-e, the lattices fringes (101) measurement is 0.287 nm

430   for NOC-ZnO[400] a lower value compared to 0.295 nm determined for TF-ZnO[400]. A

431   possible reason of that is a carbon doping in the ZnO and the XRD position (101) has

432   slightly blue shift. Meanwhile, the lattices fringes (101) of TOC-ZnO[400] have reduced

433   to 0.262 nm, that is mainly caused by the presence of abundant oxygen defects in the

434   ZnO (Liu et al., 2014). Very importantly, at the highest magnification, a thin layer of

435   disorder carbon with thickness ≈ 1-3 nm, can be identified especially in boundary area

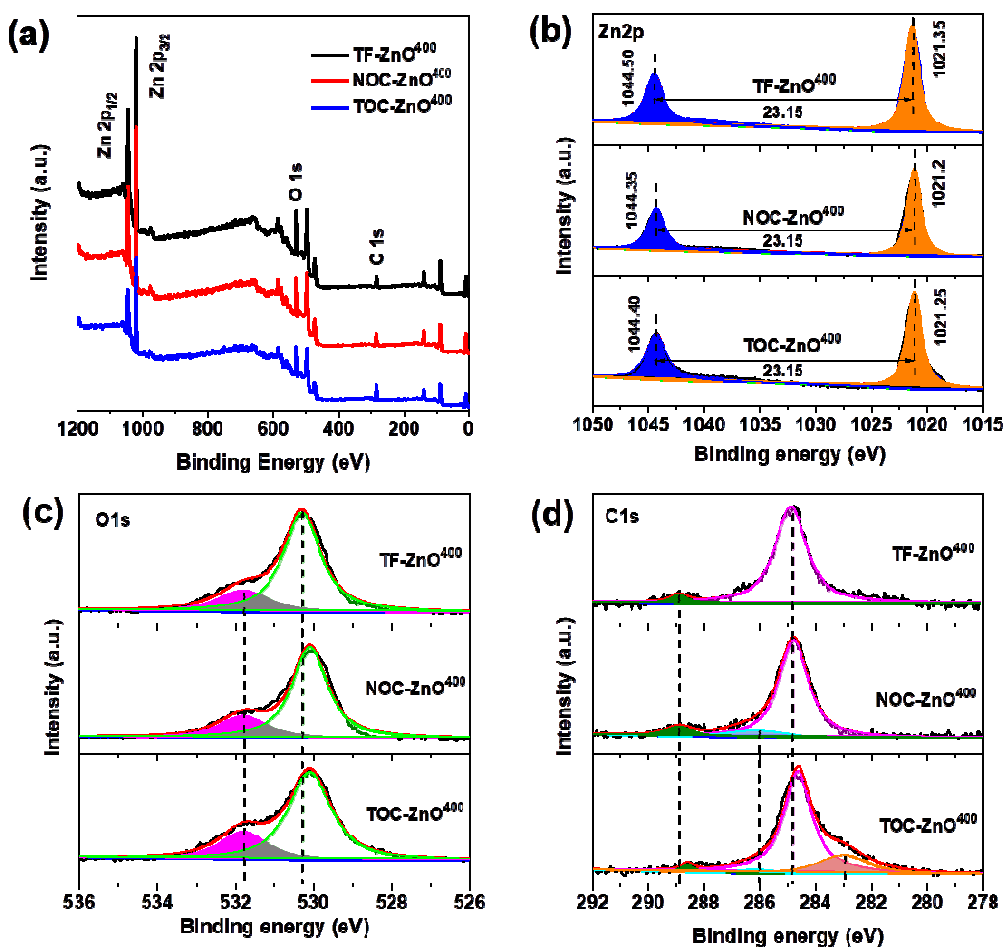436   and surrounding the dense ZnO particles.

437

Fig.6 XPS data of TF-ZnO[400], NOC-ZnO[400] and TOC-ZnO[400] samples: survey scan (a) and core

spectra with deconvolution for Zn-2p, (b) O-1s, (c) C-1s, (d).

To confirm the elemental composition and chemical states of the samples, XPS

spectra are reported in Figure 6 for samples calcined at 400°C. Two peaks at 1021.35

eV and 1044.50 eV are attributed to Zn $2p_{3/2}$ and Zn $2p_{1/2}$ levels of Zn(II). For the

NOC-ZnO[400] and TOC-ZnO[400], these binding energies are slightly negatively shifted,

which is due to the different chemical interactions(Ansari, Ansari, Foaud & Cho,

2017). Besides, the binding energies gap between Zn $2p_{3/2}$ and Zn $2p_{1/2}$ of all the ZnO

samples are similar at 23.15 eV, a clear indication that the Zn atoms are in a

449   completely oxidized state. For O1s (Figure 6-c), deconvolution leads to two signals

450   one binding energy at 531.8 eV corresponding to -OH group and one at ~530.3 eV

451   corresponding to lattice oxygen Zn-O(Kotsis & Staemmler, 2006). The latter, in the

452   case of NOC-ZnO^{400} and TOC-ZnO^{400} is 0.2 eV lower because of chemical

453   interactions present in the samples(Ansari, Ansari, Foaud & Cho, 2017). As

454   summarized in Table S4, the content of the hydroxyl group for NOC-ZnO^{400} and

455   TOC-ZnO^{400} is slightly higher than in TF-ZnO^{400}. Meanwhile, the content of lattice

456   oxygen decreased relatively. The C1s high resolution spectra of TF-ZnO^{400} can be

457   divided into two peaks at 288.90 eV and 284.90 eV, while those of NOC-ZnO^{400} and

458   TOC-ZnO^{400} can be deconvoluted into three peaks (288.90 eV, 286.10 eV and 284.80

459   eV) and four peaks (288.60 eV, 286.10 eV, 284.65 eV and 283.00 eV) shown in Table

460   S5. For all the samples, the peaks located at ~288.90 eV and ~284.90 eV could be

461   assigned to the adsorbed CO_2 and graphitic sites (forming C-C group),

462   respectively(Pan et al., 2016). The satellite peak centered at 283.0 eV might be

463   attributed to the O-Zn-C bonds because of the presence of oxygen

464   vacancies(Alshammari et al., 2015; Mishra et al., 2013) and the peaks at 286.10 eV

465   for NOC-ZnO^{400} and TOC-ZnO^{400} might be attributed to Zn-O-C bonds(Zhang et al.,

466   2015a).

467

468   *Evaluation of the photocatalytic activity.* The photocatalytic activities of all the

469   samples were evaluated by photodegradation of methyl orange (MO) under UV light

470   irradiation. From figure 7-a and Table S6, the adsorption of MO on all the samples

471   were less than 3% after a 30 min dark adsorption. From a general point of view, the

472   photocatalytic activity follows the order TOC-ZnO^{400} > NOC-ZnO^{400} > TOC-ZnO^{300} >

473   TF-ZnO^{400} > TOC-ZnO^{500} > TOC-ZnO^{600}. After 120 min of photodegradation, 95.4%

474   of MO was removed by TOC-ZnO^{400}, while the NOC-ZnO^{400} and TF-ZnO^{400} only

475   degraded 74.8% and 65.9% of MO, respectively. Besides, photodegradation of MO by

476   TF-ZnO, NOC-ZnO and TOC-ZnO before calcination was only respectively 5.4%,

477   6.8% and 7.5% after 120 min UV light irradiation in Fig.S5, which shows that proper

478   calcination treatment improves the photocatalytic activities by the conversion of the

479   Zinc(II) hydroxocarbonate into ZnO, and by enhancing the crystallinity of the

480   material. Figure 7-b displays that photocatalytic rate of TOC-ZnO^{400} was up to

481   2.54×10^{-2} min^{-1}, which is 2.2 times and 2.9 times that of NOC-ZnO^{400} and TF-ZnO^{400}.

482   This can be partially correlated with the higher specific surface area of TOC-ZnO^{400}

483   (see Table S3) the rate constants ($k^{'}_{app}$) for TOC-ZnO^{400} being both 1.3 times that of

484   TF-ZnO^{400} and NOC-ZnO^{400} (see Table S6). Importantly, this set of data points out

485   that there is an optimum for the temperature of calcination, indeed rate constants for

486   ZnO annealed at lower (300°) or higher (500 and 600°C) temperature are $<1 \times 10^{-2}$

487   min^{-1}, lower than the one for a calcination performed at 400°C. Compared with other

488   reported literatures in Table 1, TOC-ZnO^{400} appears as a very attractive materials

489   avoiding the use of leachable heavy metal like Cu and very efficient a very low
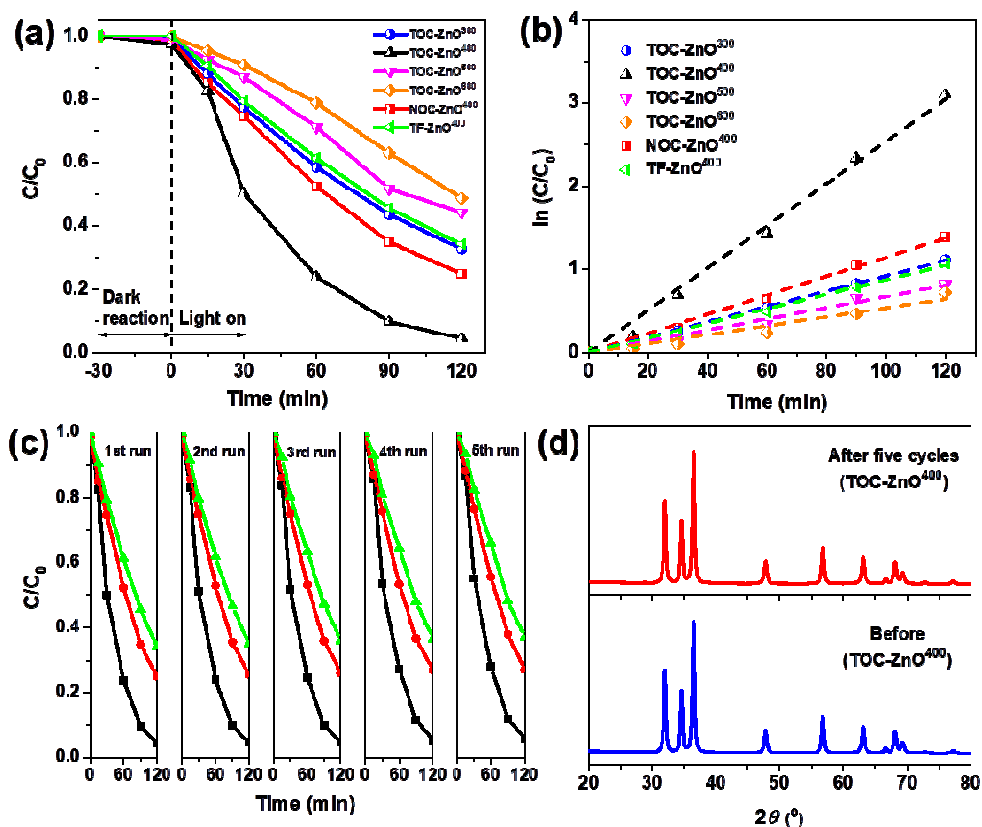
490   concentration (0.25 mg L^{-1}).

Fig.7 Photocatalytic degradation curves of methyl orange by different ZnO^x samples (a) and (b); reusability assessment of TF-ZnO^{400} (▲), NOC-ZnO^{400} (●) and TOC-ZnO^{400} (■) for methyl orange photodegradation (c); XRD patterns of TOC-ZnO^{400} before and after photocatalytic application for methyl orange (d).

Table 1 Comparison of photocatalytic activity of TEMPO-oxidized cellulose-derived carbon coated/doped ZnO with other recently reported ZnO photocatalysts

No.	ZnO samples	Cata. conc. (g L^{-1})	Degra. conc. (mg L^{-1})	Cata./ degra. (g/g)	UV-ir. (min)	Degra. (%)	Ref.
1	ZnO	0.5	10 (MO)	50	180	96.5	(Li, Lu & Luo, 2017)
2	ZnO	1.5	20 (MO)	75	100	81	(Gawade, Gavade, Shinde, Babar, Kadam & Garadkar, 2017)
3	ZnO	2	10 (MO)	200	210	92	(Kumar, Kumar & Umar,

							2013)
4	Cu-ZnO	0.5	10 (MO)	50	90	99.7	(Kadam, Kim, Shin, Garadkar & Park, 2017)
5	Al-ZnO	4	10 (MO)	400	120	95	(Lee, Kim, Park, Hong & Lee, 2015)
6	C-ZnO	0.4	4.8 (MB)	83.3	60	83	(Lee, Lim, Kang & Suh, 2015)
7	C-ZnO	2.5	5 (MB)	500	120	98	(Zhao, Zuo, Guo & Pan, 2017)
8	TOC-ZnO^{400}	0.25	5 (MO)	50	120	95.4	This work

499

500   Photocatalytic reusability of TOC-ZnO^{400}, NOC-ZnO^{400} and TF-ZnO^{400} were

501   investigated by reusing the catalysis in consecutive MO degradation reactions under

502   UV-irradiation. Before reuse, the catalysts were only washed with deionized water

503   and vacuum dried at 40ºC. Figure 7-c displays that TOC-ZnO^{400}, NOC-ZnO^{400} and

504   TF-ZnO^{400} exhibit total photocatalytic durability after five cycles. Characterization by

505   XRD demonstrated the absence of structural change for TOC-ZnO^{400} before and after

506   photocatalytic performance (Figure 7-d).
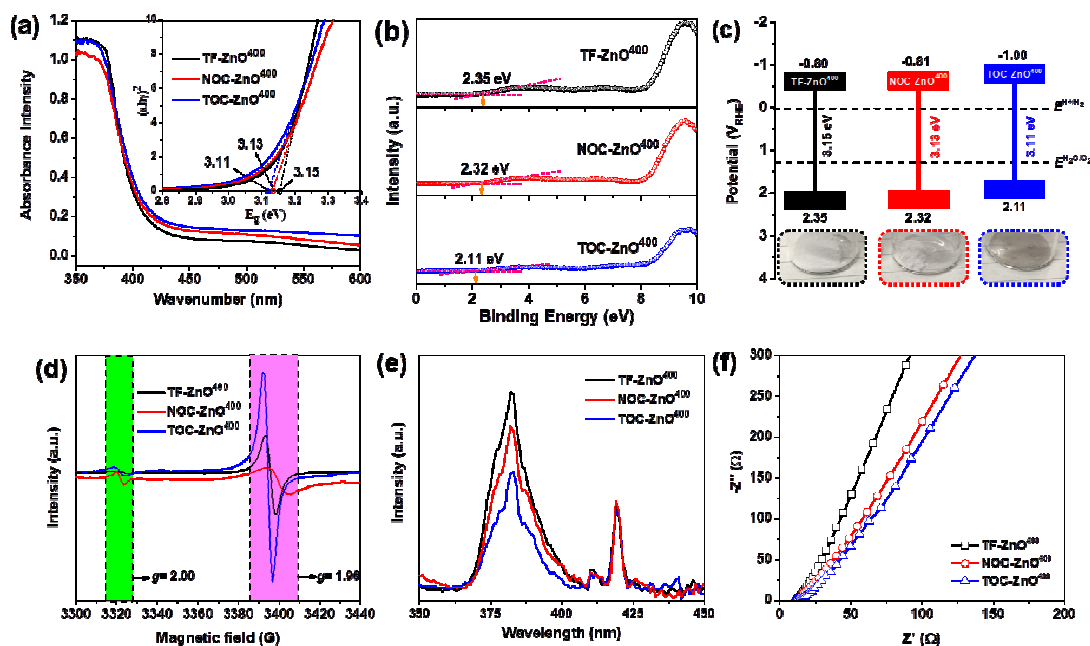
507

508   **Fig.8** Characterization of TF-ZnO^{400}, NOC-ZnO^{400} and TOC-ZnO^{400} by UV-vis DRS (a), XPS

509   spectra of all the samples for VB positions (b), VB and CB positions of all the samples (c), EPR

510   spectra (d), PL spectra (e) and EIS Nyquist plot (f).

511

512   *Photocatalytic mechanism.* To explore the mechanism of the photocatalytic activity of

513   carbon-coated ZnO obtained by calcination at 400°C, the band structures of

514   TF-ZnO[400], NOC-ZnO[400] and TOC-ZnO[400] have been probed. From Figure 8-a, the

515   UV-vis diffuse reflectance spectra of all the samples exhibited absorption in the UV

516   region (<400 nm). Compared with TF-ZnO[400], NOC-ZnO[400] and TOC-ZnO[400] have a

517   slightly red shifted absorption and possibly possess absorbance in the visible light

518   region, which is ascribed at present to the carbon doping of the ZnO nanocrystals(Jiao

519   et al., 2017; Zhang et al., 2015b). For the direct semiconductor ZnO, the band gap

520   energy was determined based on Tauc's equation(Shah et al., 2018):

521    $$\alpha h\gamma = A(h\gamma - E_g)^2$$

522   where α, A, γ, and E_g is the absorption coefficient, proportionality constant, light

523   frequency and band gap energy, respectively. From Figure 8-b, the band gap of

524   TF-ZnO[400], NOC-ZnO[400] and TOC-ZnO[400] are respectively 3.15 , 3.13 and 3.11 eV. In

525   order to measure the positions of conductive band (CB) and valence band (VB),

526   valence band potentials of all the samples were firstly detected by XPS

527   characterization. From Figure 8-b, the VB values of TF-ZnO[400], NOC-ZnO[400] and

528   TOC-ZnO[400] were 2.35 eV, 2.32 eV and 2.11 eV, respectively, which was obtained

529   from tangent lines with XPS spectra. Thus, according to the formula ($E_g = VB - CB$), CB

530   values of TF-ZnO[400], NOC-ZnO[400] and TOC-ZnO[400] were -0.80 eV, -0.81 eV and

531   -0.10 eV, respectively. CB and VB positions of all the samples are displayed in Figure

532   8-c; ZnO templated by cellulose, especially by TOC template, had shifted to the lower

533   potentials with a narrower band.

534   EPR spectra were recorded in order to evaluate different defects (such as

535   vacancies and interstitials) in ZnO through detecting the unpaired electron spins(Lv,

536   Yao, Ma, Pan, Zong & Zhu, 2013). Oxygen vacancy is one of the important surface

537   defects which can be caused by atom(C)-doping or appropriate thermal

538   treatment(Polarz et al., 2006; Schneider et al., 2009) and Zinc interstitials (called Zn_i)

539   is the other defect due to the incomplete annealing of the precursor(Zeng, Duan, Li,

540   Yang, Xu & Cai, 2010). Both defects are important features of the material since it is

541   known that such surface defects modify and possibly favor the adsorption and

542   photocatalytic activities of catalysts. EPR spectra in Figure 8-d reveal different signals

543   of the TF-ZnO^{400}, NOC-ZnO^{400} and TOC-ZnO^{400} ascribed to two kinds of defects in

544   ZnO nanocrystals, namely zinc interstitials (Zn_i, g=1.96)(McCluskey & Jokela, 2009;

545   Selim, Weber, Solodovnikov & Lynn, 2007) and oxygen vacancies (V_o,

546   g=2.00)(Polarz et al., 2006). As shown in Figure 8-d, on the one hand, TOC-ZnO^{400}

547   and NOC-ZnO^{400} are assumed to have higher intensities of oxygen vacancy than

548   TF-ZnO^{400}, because of carbon associated with the ZnO nanocrystals, which is also in

549   accordance with the XPS spectra. Abundant oxygen vacancies in the ZnO could

550   further reduce the band gap in order to enhance the photocatalytic activity(Liu et al.,

551   2014). On the other hand, the content of zinc interstitials of TOC-ZnO^{400} is

552   significantly higher than TF-ZnO^{400} and NOC-ZnO^{400}, which might be ascribed to the

553   new bond formation of O-Zn-C as shown in Table S5. Besides, it is assumed that the

554   abundant oxygen defects and zinc interstitials also built enough vacancies and

555   exposed more active sites in order to enhance the photocatalytic activities(Kayaci,

556   Vempati, Donmez, Biyikli & Uyar, 2014; Wang et al., 2012).

557   In the photocatalytic processes, the majority of light absorption and subsequent

558   photo-excitation are usually generated on the surface of the photocatalyst, then

559   leading to the transfer and/or recombination of photo-induced electrons and holes.

560   Photoluminescence (PL) can be used to evaluate the separation or recombination rates

561   of photo-generated electron-hole carriers. A weak PL intensity reflects a low

562   recombination of photo-generated electron-hole carriers. From Figure 8-e, TF-ZnO^{400}

563   exhibited the strongest intensity and the PL intensity decreased in the order TF-ZnO^{400},

564   NOC-ZnO^{400} and TOC-ZnO^{400}. Although this difference can result from different

565   phenomenon, it is clear here that the increasing carbon and defect contents in the

566   samples are concomitant with a decrease of the PL intensity(Ansari, Ansari, Foaud &

567   Cho, 2017; Chen, Pang, An, Dittrich, Fan & Li, 2019). Although this C-content and

568   zinc/oxygen defects seem to reduce the recombination rates and enhance the

569   photocatalytic performance, the precise physical mechanism is not clear at present. In

570   order to get more evidences of such hypothesis, we compare the differences of

571   electron conductivity of the three samples in order to explain the transfer behavior of

572   photo-induced electrons. Electrochemical impedance spectroscopy (EIS) of ZnO

573   samples (Figure 8-f) was measured to go deeper in understanding the behavior of the

574   material and, eventually explain the difference inphotocatalytic activities. The slope of

32

575   EIS curve of TOC-ZnO^{400} is lower than NOC-ZnO^{400} and TF-ZnO^{400}, which indicated

576   that the former had higher electron transfer efficiency that can be ascribed to the

577   C-layer coating on the surface of the ZnO, significantly increasing electron transfer.

578   Thanks to fast transportation of photo-generated electrons, TOC-ZnO^{400} shows the

579   lowest PL intensity resulting from recombination of photo-generated electron-hole

580   carriers discussed above. Besides, it is known that carbon layer could adsorb more

581   ultraviolet and visible light yielding more photo-generated carriers (such as holes and

582   electrons). On the other hand, the doping of carbon in the ZnO lattice leads to the

583   formation of new mid-gap energy states above the valence band of O_{2p} orbitals of

584   ZnO mainly because of the existence of oxygen vacancies and causing to the

585   reduction of VB value(Alshammari et al., 2015; Liu et al., 2014). Above all, due to the

586   co-function of carbon coating and doping, the band gap of ZnO decreases and light

587   absorptions has a red-shift, which is favorable to the generated electrons easily

588   migrating to the conduction band. The photocatalytic reaction mechanism was shown
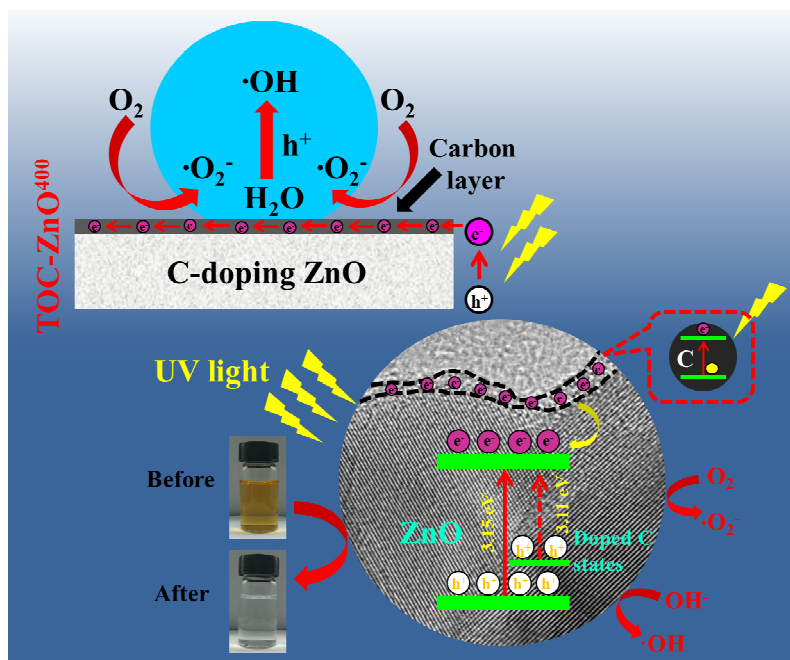
589   in Figure 9.

590

Fig.9 Schematic illustration of the possible photocatalytic reaction mechanism of C-coated ZnO

obtained from TEMPO-oxidized cellulose.

Conclusions

This study introduces new elements on the great versatility of the use of cellulose as a

sacrificial biotemplate for the preparation of metal oxide/C functional nanocomposites

by hydrothermal process. It confirms that carboxyl-content control the morphology,

microstructures and particles size of the metal oxide, ZnO in the present case. We also

show that pyrolysis is not necessary to achieve the presence of nanocarbon associated

with ZnO, this can also be obtained by a careful control of the calcination of cellulose.

Concerning the photocatalytic activity of these materials, it is demonstrated that a thin

carbon layer onto ZnO increases the charge transfer and hydrophobicity of ZnO, a

narrowing of ZnO band gap and an increase of the zinc (V_{Zn}) and oxygen (V_o)

vacancies effectively suppressing of the charge recombination.

References

Abouzeid, R. E., Khiari, R., Beneventi, D., & Dufresne, A. (2018). Biomimetic mineralization of three-dimensional printed alginate/TEMPO-Oxidized cellulose nanofibril scaffolds for bone tissue engineering. *Biomacromolecules, 19*(11), 4442-4452.

Ali, A., Ambreen, S., Maqbool, Q., Naz, S., Shams, M. F., Ahmad, M., Phull, A. R., & Zia, M. (2016). Zinc impregnated cellulose nanocomposites: synthesis, characterization and applications. *Journal of Physics and Chemistry of Solids, 98*, 174-182.

Alshammari, A. S., Chi, L. N., Chen, X. P., Bagabas, A., Kramer, D., Alromaeh, A., & Jiang, Z. (2015). Visible-light photocatalysis on C-doped ZnO derived from polymer-assisted pyrolysis. *RSC Advances, 5*(35), 27690-27698.

Ansari, S. A., Ansari, S. G, Foaud, H., & Cho, M. H. (2017). Facile and sustainable synthesis of carbon-doped ZnO nanostructures towards the superior visible light photocatalytic performance. *New Journal of Chemistry, 41*(17), 9314-9320.

Beltran, J. J., Barrero, C. A., & Punnoose, A. (2019). Relationship between

ferromagnetism and formation of complex carbon bonds in carbon doped ZnO powders. *Physical Chemistry Chemical Physics, 21*(17), 8808-8819.

Boury, B., & Plumejeau, S. (2015). Metal oxides and polysaccharides: an efficient hybrid association for materials chemistry. *Green Chemistry, 17*(1), 72-88.

Cao, X., Ding, B., Yu, J., & Al-Deyab, S. S. (2012). Cellulose nanowhiskers extracted from TEMPO-oxidized jute fibers. *Carbohydrate Polymers, 90*(2), 1075-1080.

Chen, R., Pang, S., An, H., Dittrich, T., Fan, F., & Li, C. (2019). Giant defect-induced effects on nanoscale charge separation in semiconductor photocatalysts. *Nano Letters, 19*(1), 426-432.

Cheng, J., Ma, J., Ma, Y., Zhou, C., Qiang, Y., Zhou, X., Yang, J., Shi, H., & Xie, Y. (2018). Highly efficient ZnO-based dye-sensitized solar cells with low-cost Co-Ni/carbon aerogel composites as counter electrodes. *New Journal of Chemistry, 42*(19), 16329-16334.

Cheng, Q., Ji, L., Wu, K., & Zhang, W. (2016). Morphology-dependent electrochemical enhancements of porous carbon as sensitive determination platform for ascorbic acid, dopamine and uric acid. *Scientific Reports, 6*.

Cullity, B. D. (1978). Elements of X-ray diffraction. *Addison-Wesley Publishing Company, Inc.,* 2: 248.

Dong, S., Feng, J., Fan, M., Pi, Y., Hu, L., Han, X., Liu, M., Sun, J., & Sun, J. (2015). Recent developments in heterogeneous photocatalytic water treatment using visible light-responsive photocatalysts: a review. *RSC Advances, 5*(19), 14610-14630.

Foresti, M. L., Vazquez, A., & Boury, B. (2017). Applications of bacterial cellulose as precursor of carbon and composites with metal oxide, metal sulfide and metal nanoparticles: A review of recent advances. *Carbohydrate Polymers, 157*, 447-467.

Gawade, V. V., Gavade, N. L., Shinde, H. M., Babar, S. B., Kadam, A. N., & Garadkar, K. M. (2017). Green synthesis of ZnO nanoparticles by using Calotropis procera leaves for the photodegradation of methyl orange. *Journal of Materials Science-Materials in Electronics, 28*(18), 14033-14039.

Han, C., Yang, M.-Q., Weng, B., & Xu, Y.-J. (2014). Improving the photocatalytic activity and anti-photocorrosion of semiconductor ZnO by coupling with versatile

661   carbon. *Physical Chemistry Chemical Physics, 16*(32), 16891-16903.

662   Hewlett, R. M., & McLachlan, M. A. (2016). Surface structure modification of ZnO

663   and the impact on electronic properties. *Advanced Materials, 28*(20), 3893-3921.

664   Hong, S. K., Lee, J. H., & Ko, W. B. (2011). Synthesis of 60 fullerene-ZnO

665   nanocomposite under electric furnace and pPhotocatalytic degradation of organic dyes.

666   *Journal of Nanoscience and Nanotechnology, 11*(7), 6049-6056.

667   Isogai, A., Saito, T., & Fukuzumi, H. (2011). TEMPO-oxidized cellulose nanofibers.

668   *Nanoscale, 3*(1), 71-85.

669   Jiang, F., & Hsieh, Y. L. (2013). Chemically and mechanically isolated nanocellulose

670   and their self-assembled structures. *Carbohydrate Polymers, 95*(1), 32-40.

671   Jiao, J., Wei, Y., Zhao, Y., Zhao, Z., Duan, A., Liu, J., Pang, Y., Li, J., Jiang, G., &

672   Wang, Y. (2017). AuPd/3DOM-TiO_2 catalysts for photocatalytic reduction of CO_2:

673   high efficient separation of photogenerated charge carriers. *Applied Catalysis B:*

674   *Environmental, 209*, 228-239.

675   Kadam, A. N., Kim, T. G., Shin, D. S., Garadkar, K. M., & Park, J. (2017).

676   Morphological evolution of Cu doped ZnO for enhancement of photocatalytic activity.

677   *Journal of Alloys & Compounds, 710*, 102-113.

678   Kayaci, F., Vempati, S., Donmez, I., Biyikli, N., & Uyar, T. (2014). Role of zinc

679   interstitials and oxygen vacancies of ZnO in photocatalysis: a bottom-up approach to

680   control defect density. *Nanoscale, 6*(17), 10224-10234.

681   Kotsis, K., & Staemmler, V. (2006). Ab initio calculations of the O1s XPS spectra of

682   ZnO and Zn oxo compounds. *Physical Chemistry Chemical Physics, 8*(13),

683   1490-1498.

684   Kumar, R., Kumar, G., & Umar, A. (2013). ZnO nano-mushrooms for photocatalytic

685   degradation of methyl orange. *Materials Letters, 97*, 100-103.

686   Lee, H. J., Kim, J. H., Park, S. S., Hong, S. S., & Lee, G. D. (2015). Degradation

687   kinetics for photocatalytic reaction of methyl orange over Al-doped ZnO

688   nanoparticles. *Journal of Industrial & Engineering Chemistry, 25*, 199-206.

689   Lee, J., Lim, H. S., Kang, Y. S., & Suh, K. D. (2015). Carbon-doped ZnO submicron

690   spheres functionalized with carboxylate groups and effect of dispersion stability in the

colloidal system for high photocatalytic activity. *RSC Advances, 5*(126), 104556-104562.

Lee, K. M., Lai, C. W., Ngai, K. S., & Juan, J. C. (2016). Recent developments of zinc oxide based photocatalyst in water treatment technology: A review. *Water Research, 88*, 428-448.

Lefatshe, K., Muiva, C. M., & Kebaabetswe, L. P. (2017). Extraction of nanocellulose and in-situ casting of ZnO/cellulose nanocomposite with enhanced photocatalytic and antibacterial activity. *Carbohydrate Polymers, 164*, 301-308.

Li, B., & Cao, H. (2011). ZnO@graphene composite with enhanced performance for the removal of dye from water. *Journal of Materials Chemistry, 21*(10), 3346-3349.

Li, J. Y., Lan, L., JianPing, X., XiaoSong, Z., HaiYan, L., & JinYan, Z. Controlled growth of ZnO nanorods by polymer template and their photoluminescence properties. *Science in China, 52*(4), 888-892.

Li, P., Lu, B., & Luo, Z. (2017). Hydrothermal growth of wheatear-shaped ZnO microstructures and their photocatalytic activity. *Bulletin of Materials Science, 40*(6), 1069-1074.

Liu, D., Lv, Y., Zhang, M., Liu, Y., Zhu, Y., Zong, R., & Zhu, Y. (2014). Defect-related photoluminescence and photocatalytic properties of porous ZnO nanosheets. *Journal of Materials Chemistry A, 2*(37), 15377-15388.

Liu, S., Yao, K., Wang, B., & Ma, M.-G. (2017). Microwave-assisted hydrothermal synthesis of cellulose/ZnO composites and its thermal transformation to ZnO/carbon composites. *Iranian Polymer Journal, 26*(9), 681-691.

Lv, Y., Yao, W., Ma, X., Pan, C., Zong, R., & Zhu, Y. (2013). The surface oxygen vacancy induced visible activity and enhanced UV activity of a ZnO_{1-x} photocatalyst. *Catalysis Science & Technology, 3*(12), 3136-3146.

McCluskey, M. D., & Jokela, S. J. (2009). Defects in ZnO. *Journal of Applied Physics, 106*(7), 071101.

Mishra, D. K., Mohapatra, J., Sharma, M. K., Chattarjee, R., Singh, S. K., Varma, S., Behera, S. N., Nayak, S. K., & Entel, P. (2013). Carbon doped ZnO: synthesis, characterization and interpretation. *Journal of Magnetism and Magnetic Materials,*

329, 146-152.

O'Connell, D. W., Birkinshaw, C., & O'Dwyer, T. F. (2008). Heavy metal adsorbents prepared from the modification of cellulose: A review. *Bioresource Technology, 99*(15), 6709-6724.

Olaru, N., Calin, G., & Olaru, L. (2014). Zinc oxide nanocrystals grown on cellulose acetate butyrate nanofiber mats and their potential photocatalytic activity for dye degradation. *Industrial & Engineering Chemistry Research, 53*(46), 17968-17975.

Olivera, S., Muralidhara, H. B., Venkatesh, K., Guna, V. K., Gopalakrishna, K., & Kumar, Y. K. (2016). Potential applications of cellulose and chitosan nanoparticles/composites in wastewater treatment: A review. *Carbohydrate Polymers, 153*, 600-618.

Pan, L., Muhammad, T., Ma, L., Huang, Z. F., Wang, S. B., Wang, L., Zou, J. J., & Zhang, X. W. (2016). MOF-derived C-doped ZnO prepared via a two-step calcination for efficient photocatalysis. *Applied Catalysis B-Environmental, 189*, 181-191.

Patrinoiu, G., Calderon-Moreno, J. M., Birjega, R., Culita, D. C., Somacescu, S., Musuc, A. M., Spataru, T., & Carp, O. (2016). Sustainable one-pot integration of ZnO nanoparticles into carbon spheres: manipulation of the morphological, optical and electrochemical properties. *Physical Chemistry Chemical Physics, 18*(44), 30794-30807.

Pierre, G., Punta, C., Delattre, C., Melone, L., Dubessay, P., Fiorati, A., Pastori, N., Galante, Y. M., & Michaud, P. (2017). TEMPO-mediated oxidation of polysaccharides: An ongoing story. *Carbohydrate Polymers, 165*, 71-85.

Polarz, S., Strunk, J., Ischenko, V., van den Berg, M. W. E., Hinrichsen, O., Muhler, M., & Driess, M. (2006). On the role of oxygen defects in the catalytic performance of zinc oxide. *Angewandte Chemie International Edition, 45*(18), 2965-2969.

Qu, Y., & Duan, X. (2013). Progress, challenge and perspective of heterogeneous photocatalysts. *Chemical Society Reviews, 42*(7), 2568-2580.

Safwat, E., Hassan, M. L., Saniour, S., Zaki, D. Y., Eldeftar, M., Saba, D., & Zazou, M. (2018). Injectable TEMPO-oxidized nanofibrillated cellulose/biphasic calcium phosphate hydrogel for bone regeneration. *Journal of Biomaterials Applications,*

751 *32*(10), 1371-1381.

752 Samadi, M., Shivaee, H. A., Zanetti, M., Pourjavadi, A., & Moshfegh, A. (2012).

753 Visible light photocatalytic activity of novel MWCNT-doped ZnO electrospun

754 nanofibers. *Journal of Molecular Catalysis a-Chemical, 359*, 42-48.

755 Schneider, J. J., Hoffmann, R. C., Engstler, J., Dilfer, S., Klyszcz, A., Erdem, E., Jakes,

756 P., & Eichel, R. A. (2009). Zinc oxide derived from single source precursor chemistry

757 under chimie douce conditions: formation pathway, defect chemistry and possible

758 applications in thin film printing. *Journal of Materials Chemistry, 19*(10), 1449-1457.

759 Sehaqui, H., Zhou, Q., Ikkala, O., & Berglund, L. A. (2011). Strong and tough

760 cellulose nanopaper with high specific surface area and porosity. *Biomacromolecules,*

761 *12*(10), 3638-3644.

762 Selim, F. A., Weber, M. H., Solodovnikov, D., & Lynn, K. G. (2007). Nature of native

763 defects in ZnO. *Physical Review Letters, 99*(8), 085502.

764 Shah, N. S., Khan, J. A., Sayed, M., Khan, Z. U., Rizwan, A. D., Muhammad, N.,

765 Boczkaj, G., Murtaza, B., Imran, M., Khan, H. M., & Zaman, G. (2018). Solar light

766 driven degradation of norfloxacin using as-synthesized Bi^{3+} and Fe^{2+} co-doped ZnO

767 with the addition of HSO_5^- : Toxicities and degradation pathways investigation.

768 *Chemical Engineering Journal, 351*, 841-855.

769 Spathis, P. P., I. (1995). The corrosion and photocorrosion of zinc and zinc oxide

770 coatings. *Corrosion Science, 37*(5), 673-680.

771 Tran, D. T. (2016). Synthesis of porous ZnO based materials using an agarose gel

772 template for H_2S desulfurization. *RSC Advances, 6*(2), 1339-1345.

773 Vaiano, V., Matarangolo, M., Murcia, J. J., Rojas, H., Navio, J. A., & Hidalgo, M. C.

774 (2018). Enhanced photocatalytic removal of phenol from aqueous solutions using

775 ZnO modified with Ag. *Applied Catalysis B-Environmental, 225*, 197-206.

776 Wang, J., Wang, Z., Huang, B., Ma, Y., Liu, Y., Qin, X., Zhang, X., & Dai, Y. (2012).

777 Oxygen vacancy induced band-Gap narrowing and enhanced visible light

778 photocatalytic activity of ZnO. *ACS Applied Materials & Interfaces, 4*(8), 4024-4030.

779 Wu, X., Lu, C., Zhang, W., Yuan, G., Xiong, R., & Zhang, X. (2013). A novel

780 reagentless approach for synthesizing cellulose nanocrystal-supported palladium

781 nanoparticles with enhanced catalytic performance. *Journal of Materials Chemistry A,*

782 *1*(30), 8645-8652.

783 Xiao, H., Zhang, W., Wei, Y., & Chen, L. (2018). Carbon/ZnO nanorods composites

784 templated by TEMPO-oxidized cellulose and photocatalytic activity for dye

785 degradation. *Cellulose, 25*(3), 1809-1819.

786 Xiong, R., Lu, C., Wang, Y., Zhou, Z., & Zhang, X. (2013). Nanofibrillated cellulose

787 as the support and reductant for the facile synthesis of Fe_3O_4/Ag nanocomposites with

788 catalytic and antibacterial activity. *Journal of Materials Chemistry A, 1*(47),

789 14910-14918.

790 Yang, M.-Q., Weng, B., & Xu, Y.-J. (2013). Improving the visible light photoactivity

791 of In_2S_3-graphene nanocomposite via a simple surface charge modification approach.

792 *Langmuir, 29*(33), 10549-10558.

793 Yang, M.-Q., Weng, B., & Xu, Y.-J. (2014). Synthesis of In_2S_3-CNT nanocomposites

794 for selective reduction under visible light. *Journal of Materials Chemistry A, 2*(6),

795 1710-1720.

796 Yang, M.-Q., & Xu, Y.-J. (2013). Basic principles for observing the photosensitizer

797 role of graphene in the graphene-semiconductor composite photocatalyst from a case

798 study on graphene-ZnO. *Journal of Physical Chemistry C, 117*(42), 21724-21734.

799 Ye, S., Zhang, D., Liu, H., & Zhou, J. (2011). ZnO nanocrystallites/cellulose hybrid

800 nanofibers fabricated by electrospinning and solvothermal techniques and their

801 photocatalytic activity. *Journal of Applied Polymer Science, 121*(3), 1757-1764.

802 Yu, H.-Y., Chen, G.-Y., Wang, Y.-B., & Yao, J.-M. (2015). A facile one-pot route for

803 preparing cellulose nanocrystal/zinc oxide nanohybrids with high antibacterial and

804 photocatalytic activity. *Cellulose, 22*(1), 261-273.

805 Yu, W., Zhang, J., & Peng, T. (2016). New insight into the enhanced photocatalytic

806 activity of N-, C- and S-doped ZnO photocatalysts. *Applied Catalysis*

807 *B-Environmental, 181*, 220-227.

808 Yuan, Y., Fu, A., Wang, Y., Guo, P., Wu, G., Li, H., & Zhao, X. S. (2017). Spray

809 drying assisted assembly of ZnO nanocrystals using cellulose as sacrificial template

810 and studies on their photoluminescent and photocatalytic properties. *Colloids and*

811   *Surfaces A-Physicochemical and Engineering Aspects, 522*, 173-182.

812   Zeng, H., Duan, G., Li, Y., Yang, S., Xu, X., & Cai, W. (2010). Blue luminescence of

813   ZnO nanoparticles based on non-equilibrium processes: defect origins and emission

814   controls. *Advanced Functional Materials, 20*(4), 561-572.

815   Zhang, X., Qin, J., Hao, R., Wang, L., Shen, X., Yu, R., Limpanart, S., Ma, M., & Liu,

816   R. (2015a). Carbon-doped ZnO nanostructures: facile synthesis and visible light

817   photocatalytic applications. *The Journal of Physical Chemistry C, 119*(35),

818   20544-20554.

819   Zhang, X. Y., Qin, J. Q., Hao, R. R., Wang, L. M., Shen, X., Yu, R. C., Limpanart, S.,

820   Ma, M. Z., & Liu, R. P. (2015b). Carbon-doped ZnO nanostructures: facile Synthesis

821   and visible light photocatalytic applications. *Journal of Physical Chemistry C,*

822   *119*(35), 20544-20554.

823   Zhang, Y., Zhang, N., Tang, Z.-R., & Xu, Y.-J. (2012). Graphene transforms wide

824   band gap ZnS to a visible light photocatalyst. the new role of graphene as a

825   macromolecular photosensitizer. *ACS Nano, 6*(11), 9777-9789.

826   Zhao, S.-W., Zuo, H.-F., Guo, Y.-R., & Pan, Q.-J. (2017). Carbon-doped ZnO aided by

827   carboxymethyl cellulose: fabrication, photoluminescence and photocatalytic

828   applications. *Journal of Alloys and Compounds, 695*, 1029-1037.

829   Zhou, P., Yu, J., & Jaroniec, M. (2014). All-solid-state Z-Scheme photocatalytic

830   systems. *Advanced Materials, 26*(29), 4920-4935.

831